

Open snake model based on global guidance field for embryo vessel location

ISSN 1751-9632

Received on 14th November 2016

Revised 14th June 2017

Accepted on 20th July 2017

E-First on 8th November 2017

doi: 10.1049/iet-cvi.2016.0411

www.ietdl.orgWeicheng Xie^{1,2}, Jinming Duan³, Linlin Shen^{1,2}✉, Yuexiang Li¹, Meng Yang¹, Guojun Lin⁴¹School of Computer Science & Software Engineering, Shenzhen University, Shenzhen 518060, People's Republic of China²Shenzhen Key Laboratory of Spatial Information Smart Sensing and Services, Shenzhen University, Shenzhen 518060, People's Republic of China³School of Computer Science, University of Nottingham, Nottingham NG81BB, UK⁴School of Automation and Electronic Information, Sichuan University of Science & Engineering, People's Republic of China

✉ E-mail: llshen@szu.edu.cn

Abstract: The development of vessels can provide important information about the growth status of animal embryos. It is, therefore, important to automatically locate the deformed vessel branches from the embryo images. However, very few vessel detectors can accurately locate all vessel branches when the captured images are low quality and the implied vessel shapes are complex. In this study, a new framework consisting of vessel region extraction and snake shape optimisation is proposed. The main contribution in this detector is a novel open snake model based on the global guidance field and deformation template initialisation. Experimental results on a specific application of an embryo vessel database [Database and source codes: <https://github.com/wcxie/Egg-embryo-vessel-location/>] demonstrate that the proposed algorithm not only locates the vessel shape properly but also obtains the orientations of embryo vessel branches accurately. Comparison to traditional guidance fields and the active appearance model illustrates the effectiveness and competitiveness of the proposed model.

1 Introduction

During the past few decades, vessel location has been widely used in vessel-related automatic analysis, which is a consistently popular research topic. Kirbas and Quek [1] classified the algorithms for blood vessel detection into six categories and provided a review of each algorithm category.

With respect to (w.r.t.) general vessel location, pattern recognition-related approaches [1] such as the skeleton method [2], self-adaptive thresholds [3] and matching filter approach [4] were often employed. While the geometric deformable models of the level-set method such as [5–8] are also applicable to extract the vessel region, they can easily introduce over-segmentation. These algorithms are applicable to predict the initial vessel region for the further optimisation. However, they do not sufficiently use the prior structure information implied in the vessel shape, thus cannot identify the vessel branch information.

Unlike unordered vessels with uncertain fragment branches such as retina vessels, there are vessels often shown with relatively fixed and ordered shape. In this case, deformation template models that incorporate the prior shape information are applicable such as ellipse shape deformation [9, 10], morphological skeleton [11] and hierarchical part-template matching [12]. However, the oversimplification of the employed shape template or the requirement for high-quality images limits their application. The active appearance model (AAM) [13] approximates the target shape with a linear combination of a training shape database, whereas the efficacy of these models is limited for vessel location since the training database is often small and the shape variation space is large.

The snake deformation model is proposed for general object location [1], which is frequently used for blood vessel detection due to its flexibility during shape optimisation. Current snake algorithms such as the classical snake model [14] locate the vessel boundary with a closed curve, which is applicable for locating the entire vessel shape. To apply the snake model to vessel branch location, open snake models for locating 3D neuron centre lines [15, 16] were proposed; these models drove seed points progressively using a deforming force combination of gradient

vector flow (GVF), stretching force and a set of control rules on the neuron structure. However, these curve-growing models may not be suitable for vessel location with incomplete branches or noisy bifurcations. In this work, rather than driving the curve progressively in the form of line segments, an open snake model is proposed to drive an initialised whole curve toward the longest skeleton N .

From another perspective, the classical snake model [14] is sensitive to noise and shape initialisation. To decrease the influence of image noise, Bresson *et al.* [17] proposed an active snake model with global optimisation based on the unification of image segmentation and image denoising tasks. To reduce the sensitivity of the classical snake model on shape initialisation and boundary concavities, Xu and Prince [18] proposed a potential force of gradient vector flow (GVF) with information regarding the distance apart from the real boundary edge to help the evolution curve converge to the boundary edge. On the basis of this, Li *et al.* [19] proposed the edge preserving GVF as the external force; Hou and Han [20] employed distance potential force distribution to improve GVF on initialisation sensitivity; and Li *et al.* [21] proposed a radiating GVF snake to facilitate the convergence of the evolution curve to the real boundary. However, in these constructed potential forces, only the information regarding the distance apart from the detected boundary edge is used, while the length of the detected edge line is not considered; thus, the evolution curve may stagnate because of the fragment edges contained in the contaminated image. In this work, a global guidance field (GGF) is proposed to make up for this deficiency that incorporates not only the distance apart from the skeleton lines but also the lengths of these skeleton lines to avoid converging to small edge fragments.

Although an improved guidance field is proposed to handle the case of initialised shapes far from the target boundary edge, a good initialisation is still necessary to further decrease the risk of converging to a local optimum [1, 18]. Motivated by the work [12, 22], a deformation template algorithm integrating prior shape information and using region and curve template matching is proposed to obtain a global initialisation aiming at a specific application in this work.

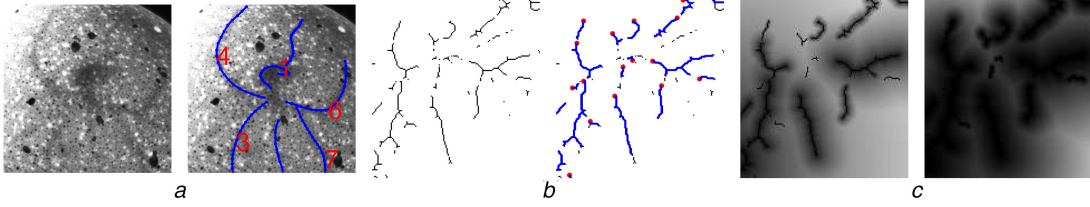


Fig. 1 Example of embryo image and the proposed guidance field (a) Example embryo image with noisy and blurry vessel shape. The left is the input embryo vessel image; the right is the shape to be located, where line 1 denotes the heart region and lines 3, 4, 6, 7 denote four main vessel branches. (b), (c): Illustration of GGF generation, (b) Skeleton centre pixels and continuous skeleton lines obtained by DFS. Red circles are the starting searching pixels, (c) Generated guidance fields with parameter $\alpha = 0.5, 1$

The real application originates from the field of biological engineering automation. According to statistics from the automated egg incubation industry, ~5–14% of the eggs do not hatch successfully within a hatching period of three weeks [23]. Therefore, researchers attempt to filter out the eggs that hatch unsuccessfully in the preceding 2 weeks and discard them in advance to save further hatching costs. Although a three-level classification of the embryo development degree was proposed for the captured images [23], the implied vessels must be further located to supervise the hatching status. However, as illustrated in Fig. 1a, the provided image contains a great deal of bright and dark spots during the imaging stage, and the embryo vessels are low contrast, which results in blurred boundaries and broken shape structures. Few algorithms can accurately locate the vessel shape and simultaneously recognise its branches when provided with such largely polluted images and vessel shapes.

In this work, given the deficiency of current vessel location algorithms for images containing blurry, bifurcated and complex vessel shapes, a framework with novel strategies for vessel region extraction and snake optimisation is proposed for location of vessels with similarly fixed shapes. The proposed framework related to the snake model consists of three novel ideas. First, an open snake model preserving curve direction and length is proposed to accurately fit the vessel skeletons. Second, a GGF is proposed for the open snake model, which employs information regarding not only the distance apart from the longest skeleton line but also the length of the corresponding skeleton line. Finally, initialisation with a deformation template method is proposed to obtain a globally initialised shape for the proposed open snake optimisation in a specific application.

This paper is structured into the following sections. The proposed framework of vessel location is presented in Section 2, which is further applied to a specific problem in Section 3. Then, the experimental results and the corresponding illustrations are demonstrated in Section 4. Finally, the conclusion and some discussions are presented in Section 5.

2 Proposed algorithm

2.1 Algorithm framework

The framework of the proposed algorithm mainly consists of shape region extraction based on self-adaptive thresholding and shape optimisation based on the proposed GGF and an open snake model.

2.2 Shape region extraction

2.2.1 Spot patching and smoothness: Owing to extra lighting sources or reflection, vessel images often contain multiple light spots. To decrease their influence, Poisson patching which is frequently used for the image inpainting [24] is employed for spot region elimination, i.e. two-dimensional (2D) Laplacian equation with Dirichlet boundary condition is used.

For the smoothness of the provided images, the minimization model of total variation regularization term with L1 norm (TVG-L1) [25] is employed to address the problem of irregular noise contained in the input images, because it can remove the anomalies and irregularities while well preserving the sharp edges of the vessel. The parameters of this algorithm are set the same as those in [25].

2.2.2 Self-adaptive thresholding: To restrict vessel shape detection in a relatively local region, the vessel shape region is extracted in advance. Since the pixel lighting intensity of a vessel is darker than that of the adjacent regions, the thresholding method [3] can be employed to filter out these pixels with different parameter settings.

The self-adaptive thresholding with the mean operator [3] transfers a grey image l into a binary image B with local threshold value tv , which is presented as

$$B_p = \begin{cases} 1 & l_p > ls(p, ws) - tv \\ 0 & \text{otherwise} \end{cases} \quad (1)$$

where l_p , B_p are the pixel values of the position p on the original and binary images and $ls(p, ws)$ is a suitable statistical operator around the position p , i.e. the mean filter. ws is the window size of the filter and tv is a user-defined threshold value.

With the filtered region, the location of vessel branches should be further improved, the following sections present the algorithms for vessel branch orientation initialisation and optimisation.

2.3 Shape optimisation with GGF-based open snake model

2.3.1 Initial shape prediction: Used before snake optimisation, shape initialisation is necessary because good initialisation largely decreases the risk of location optimisation converging to a local optimum [22]. In this work, for the proposed open snake optimisation, Section 3.2 introduces a deformation template method of shape initialisation for a specific application based on the filtered vessel region.

2.3.2 Global GF: Although the smoothed image is often employed for local optimisation in curve evolution, the small fragment noise contained in the smoothed image makes the curve vulnerable to a local optimum. In this work, GGF is proposed to facilitate local optimisation by incorporating the information related to the detected skeleton lines.

To generate GGF, the skeleton pixels are detected in the filtered vessel region using the skeletonisation algorithm [2]; continuous skeleton lines are further detected with depth-first search (DFS), where the starting pixels are selected as the upper most or lower most pixels in the estimated principal direction V_T of the vessel shape. Then, the short skeleton lines corresponding to fragmental vessel branches with length less than ϵ are abandoned to decrease the interference of noisy filtered regions. With the searched skeleton centrelines, each skeleton centre pixel is initially labelled with an intensity value, i.e. the length of the longest skeleton line across the pixel. Finally, the GGF image on each pixel p of the provided image is calculated as follows:

$$GGF_p = \min_i \frac{\| p - SP_i \|_c}{\text{Len}_{SP_i}^\alpha} \quad (2)$$

where SP_i is the i th skeleton line and Len_{SP_i} is this line's length, i.e. the same intensity value of all of the pixels on the centreline SP_i . $\| p - \mathcal{L} \|_c$ defines the distance between a point p and a curve \mathcal{L} , which is approximated as the minimum distance from the point to the dense interpolation points of the curve \mathcal{L} . Parameter α is a

balance weight, which is set to be 0.8 for all the testing. With the definition of GGF in (2), the guidance field integrates not only the distances apart from the skeleton lines but also the lengths of these lines into the shape optimisation, which can decrease the risk of converging to the fragment skeleton lines contained in the noisy images. The generated GGF is finally used to replace the conventionally used smoothed image texture for shape local optimisation, i.e. the open snake model introduced in the next section. Generation of two example guidance fields is presented in Figs. 1b and c.

(i) *Open snake model preserving direction and length*: The original snake model [14] was proposed to improve the accuracy of the located vessel boundary. However, it is not suitable for optimising the location of the open vessel branch. For the original snake model, some basic geometry features of the closed evolution curve such as curve direction and length are not preserved during curve evolution, which may result in an abnormal shape that is far away from the initial vessel branch. Thus, to propose an efficient open snake model for locating open vessel branches, some conditions must be satisfied.

- (1) The evolution curve of the snake model is open.
- (2) The direction and length of the initial branch are preserved.
- (3) The first point is fixed during snake evolving.

In the following, we introduce the proposed open snake model satisfying the above three conditions. The proposed snake model w.r.t. the variable $v(s) = (x(s), y(s))$ is represented as (see (3)) In the first term of the snake model (3), E_{int} is the internal energy, which is elaborated in the original snake model [14] and presented as follows:

$$E_{\text{int}} = \frac{1}{2}\alpha(s)\|v_s(s)\|_2^2 + \frac{1}{2}\beta(s)\|v_{ss}(s)\|_2^2 \quad (4)$$

where $v_s(s)$, $v_{ss}(s)$ are the first- and second-order derivatives w.r.t. the length variable s , reflecting the length and the blending degree of an evolution curve. Parameters $\alpha(s)$, $\beta(s)$ are the coefficients of these two derivatives, which are fixed to constants α , β to decrease the model complexity.

For the exterior energy E_{ext} in (3), the terms of E_{line} and $E_{\text{edge}} = -\|\nabla I(x, y)\|_2^2$ are retained, whereas the term reflecting the curve curvature is discarded since the vessel branch shape is smooth. That is, the exterior energy is formulated as

$$E_{\text{ext}} = \omega(E_{\text{edge}} + E_{\text{line}}) \quad (5)$$

where ω is a parameter controlling the significance of input texture image. In the original snake model, E_{line} is the image after smoothness and self-adaptive thresholding in (1), whereas it is set to be GGF image calculated in (2) of Section 2.3.2 as follows:

$$E_{\text{line}} = \text{GGF} \quad (6)$$

Since the proposed open snake model evolves an entire curve with several line segments toward the target centre line, rather than evolves stepwise line segment to trace the vessel centre line such as in [15, 16]; the two energy terms E_{DirPre} , E_{LenPre} in (3) are proposed to preserve the geometric features of the open evolution curve.

First, the energy term of vector bias E_{DirPre} reflecting the preservation degree of the initial vessel direction is proposed as follows:

$$E_{\text{DirPre}} = \frac{\theta}{2}\|v_s(s) - iv_s(s)\|_2^2 \quad (7)$$

where $iv_s(s)$ is the first derivative (vessel direction) of the initial curve before evolution.

Second, to preserve the initial arc length $\|iv_s(s)\|_2$, the energy term of distance bias E_{LenPre} is introduced as follows:

$$E_{\text{LenPre}} = \frac{\eta}{2}(\|v_s(s)\|_2 - \|iv_s(s)\|_2)^2 \quad (8)$$

With the model (3), a new open snake model using the GGF and preserving the initial geometric features of branch length and direction is proposed. To solve (3), the corresponding Euler–Lagrange condition is formulated as follows: (see (9)) where ∇E_{ext} is the gradient of the external energy E_{ext} , v_{ss} becomes a 2D vector (v_{xx}, v_{yy}) and $\nabla E_{\text{ext}} = ((\partial E_{\text{ext}}/\partial x), (\partial E_{\text{ext}}/\partial y))$ when the variable s is treated as coordinates x , y . Then, the above equation is used for the gradient descent method as follows:

$$\frac{\partial v}{\partial t} = -\delta E_{\text{snake}} \quad (10)$$

Concerning the model (10), finite difference is employed for the discretisation; i.e. $(\partial v/\partial t)$ is discretised as $\gamma(v_{i+1} - v_i)$, where $v_i = (x_i, y_i)$ and γ is the inverse of step size. Then, the model (10) is discretised as follows: (see (11)) The fourth and fifth terms on the right-hand side of (11) contain non-linear terms $(\|iv_s\|_2/\|v_s^{t+1}\|_2)v_s^{t+1}$ and $\nabla E_{\text{ext}}^{t+1}$. To make the iteration form in (11) linearly solvable, we employ the idea in [26] to make the length preservation term linear by substituting the term $(\|iv_s\|_2/\|v_s^t\|_2)v_s^t$ for $(\|iv_s\|_2/\|v_s^{t+1}\|_2)v_s^{t+1}$ and placing it on the right-hand side of the iteration equation; and similarly assume the movement of the snake is small enough that the external force does not change much from one time step to the next, yielding $\nabla E_{\text{ext}}^t \simeq \nabla E_{\text{ext}}^{t+1}$.

In (11), v_{ss}^{t+1} , v_{ssss}^{t+1} are 2D vectors $(\partial_{xx}^{t+1}x, \partial_{yy}^{t+1}y)$, $(\partial_{xxxx}^{t+1}x, \partial_{yyyy}^{t+1}y)$ when s is replaced with coordinates x , y , and $\partial_{xx}^{t+1}x = (\partial_{xx}^{t+1}x_1, \dots, \partial_{xx}^{t+1}x_n)^T$ when n is the number of the discrete points. The second-order and fourth-order spatial derivatives $\partial_{xx}x_i$ and $\partial_{xxxx}x_i$ are discretised according to the finite difference approximation under the Neumann boundary condition, then (11) is formulated as

$$(A + \gamma I)v^{t+1} = \gamma v^t - \theta \cdot iv_{ss} - \eta \frac{d}{ds} \left(\frac{\|iv_s\|_2}{\|v_s^t\|_2} v_s^t \right) - \omega \nabla E_{\text{ext}}^t \quad (12)$$

where A records the discretisation coefficients of the linear terms of v^{t+1} , iv_{ss} is the second-order derivative of the initial evolution curve iv w.r.t. the length variable s . Equation (12) w.r.t. coordinates x , y is finally re-formulated as follows: (see (13) and (14)) where $f_x = (\partial E_{\text{ext}}/\partial x)$, f_y is similarly defined. For the x coordinate of the

$$\min E_{\text{snake}} = \int_0^1 E_{\text{int}}(v(s)) + E_{\text{ext}}(v(s)) + E_{\text{DirPre}}(v(s)) + E_{\text{LenPre}}(v(s)) ds \quad (3)$$

$$\delta E_{\text{snake}} = -\alpha v_{ss} + \beta v_{ssss} - \theta(v_{ss} - iv_{ss}) - \eta \left(v_{ss} - \frac{d}{ds} \left(\frac{\|iv_s\|_2}{\|v_s^t\|_2} v_s^t \right) \right) + \omega \nabla E_{\text{ext}} = 0 \quad (9)$$

$$\gamma(v^{t+1} - v^t) = \alpha v_{ss}^{t+1} - \beta v_{ssss}^{t+1} + \theta(v_{ss}^{t+1} - iv_{ss}) + \eta \left(v_{ss}^{t+1} - \frac{d}{ds} \left(\frac{\|iv_s\|_2}{\|v_s^t\|_2} v_s^t \right) \right) - \omega \nabla E_{\text{ext}}^{t+1} \quad (11)$$

Table 1 Pseudocode of the proposed vessel location algorithm

```

1: obtain vessel filtered region with (1) and the skeleton pixels with algorithm [2]
2: parameter initialisation:  $t = 0, \alpha, \beta, \gamma, \theta, \eta, \omega, \text{NumIter}$ 
3: adopt (16)–(18) in Section 3.2 to obtain the initial shape  $v^0 = (x^0, y^0) = (ix, iy)$ 
4: use (2) to obtain GGF image  $E_{\text{line}}$  in (6)
5: while  $t < \text{NumIter}$  do
6:   use (13) and (14) to calculate the right-hand side matrix in (12)
7:   use (12) to obtain the discretised vessel points at the  $t + 1$ th iteration
8:   if (15) is satisfied, output  $v^t = (x^t, y^t)$  and exit; otherwise,  $t \leftarrow t + 1$ 
9: end while
10: if  $t = \text{NumIter}$ , output  $v^t = (x^t, y^t)$ 

```

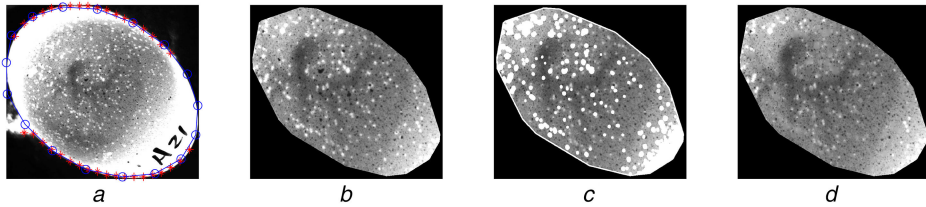


Fig. 2 Procedure of image preprocessing (a) Fitting of Canny boundary points of an original image with an ellipse. The detected boundary points are labelled with red stars and the corresponding fitted ellipse curve is labelled with blue circles, (b) Image after the erosion operation, (c) Detection result of spots with circles whose region has a perimeter $< 10\pi$ and whose average lighting intensity lies within the interval $[0.05, 0.95]$, where spots are labelled with white circles, (d) Image with white holes patched

i th point on the evolution curve, the third term on the right-hand side of (13) is computed as follows: (see (14)) where $d_i = v_{i+1} - v_i$, $id_i = iv_{i+1} - iv_i$, $v_i = (x_i, y_i)$ and $iv_i = (ix_i, iy_i)$ are the i th points on current and the initial evolution lines, respectively.

To fix the first point during the snake evolving to satisfy the third condition of the proposed model, the term related to the first point (corresponding to the first column in matrix A) is moved to the right-hand side of the iteration formula.

To decrease the risk of converging to the local optimum as well as the influence of noisy and fragment lines, the termination condition of the simulated annealing algorithm is adopted which is formulated as

$$\sum l_V^t - \sum l_V^{t-1} \geq 0.1 \sum l_V^{t-1} \quad (15)$$

where l_V^t records the lighting intensities on pixels $V = \{v_1, \dots, v_n\}$ in the t th iteration.

For clarity, the pseudocode of the entire algorithm is presented as Table 1.

3 Application of embryo vessel location

3.1 Vessel region preprocessing and extraction

In this section, the preprocessing method in Section 2.2 is employed on the chick embryo images. As illustrated in Fig. 1a, each input chick embryo image includes a vessel structure that consists of a central heart labelled with line 1 and six vessel branches labelled with green lines; the four branches labelled 3, 4, 6 and 7 and the heart shape are the target vessels that must be located.

To restrict the search range within a local region around the vessel shape, the region of interest is extracted before the spot patching in Section 2.2.1, and the preprocessing procedure is presented in Fig. 2.

With the preprocessing of the chick embryo images, TVG-L1 smoothness in Section 2.2.1 is employed to reduce the salt-and-pepper noise while preserving the vessel geometry features. Finally, self-adaptive thresholding in Section 2.2.2 is used to extract the entire embryo region with parameter setting $ws = 200$, $tv = 0.05$ for the following shape initialisation and guidance field generation.

3.2 Chick vessel shape initialisation

The basic idea of the shape initialisation is to estimate the approximated 35 points located on 7 different parts with Procrustes transformation and deformation template matching, which is conducted in three steps.

For the first step, the principal tangent and normal directions (V_T, V_N) of the central heart region are initially approximated with the first and second principal component vectors of the central heart region, which is represented in Fig. 3a.

For the second step, with the motivation from part-template matching [12], local searching with template matching is conducted around the centre point to improve the estimation of the principal directions. The basic idea of this local searching is to find the locally perturbed direction which makes the corresponding trial template region best match the filtered vessel region with the minimal lighting intensity sum SL_i as follows:

$$\begin{cases} (A + \gamma I)x^{t+1} = \gamma x^t - \theta \cdot \partial_{xx}ix - \eta \frac{\partial}{\partial x} \left(\frac{\sqrt{\partial_x ix^2 + \partial_y iy^2}}{\sqrt{(\partial_x x^t)^2 + (\partial_y y^t)^2}} \partial_x x^t \right) - \omega \cdot f_x^t \\ (A + \gamma I)y^{t+1} = \gamma y^t - \theta \cdot \partial_{yy}iy - \eta \frac{\partial}{\partial y} \left(\frac{\sqrt{\partial_x ix^2 + \partial_y iy^2}}{\sqrt{(\partial_x x^t)^2 + (\partial_y y^t)^2}} \partial_y y^t \right) - \omega \cdot f_y^t \end{cases} \quad (13)$$

$$\left[\frac{\partial}{\partial x} \left(\frac{\sqrt{\partial_x ix^2 + \partial_y iy^2}}{\sqrt{(\partial_x x^t)^2 + (\partial_y y^t)^2}} \partial_x x^t \right) \right]_i = \frac{\| id_{i+1} \|_2}{\| d_{i+1} \|_2} (x_{i+2} - x_{i+1}) - \frac{\| id_i \|_2}{\| d_i \|_2} (x_{i+1} - x_i) \quad (14)$$

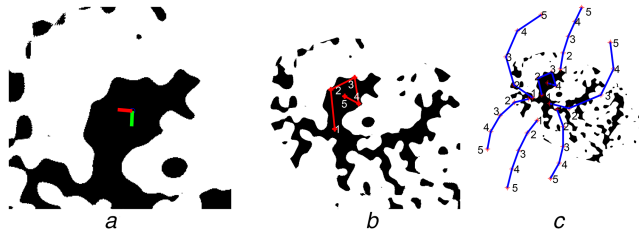


Fig. 3 Procedure of initial vessel shape generation (a) Generation of the principal tangent V_T and normal V_N directions labelled with red and green lines, (b) Five points on the heart region generated for estimating the entire shape, (c) Estimated entire vessel shape using the central five points

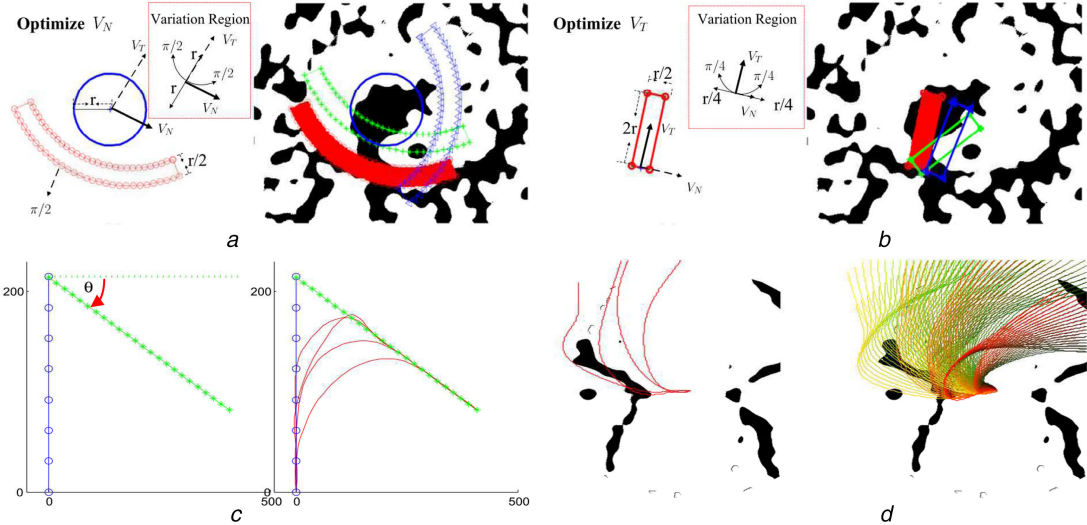


Fig. 4 Procedures of the trial template generation and the principal direction improvement (a),(b): Template region generation and local searching for principal direction improvement. Left (a): Ring template region generation for improving V_N . The top-right corner shows the variation region of the basic trial ring polygon labelled with red circles in the directions of V_T and V_N , in which the basic trial polygon is perturbed with a distance smaller than r along the direction V_T and an angle smaller than $\pi/2$ in the direction V_N . Right (a): Three example trial regions for V_N improvement. Red circles enclose the optimal trial region obtained in (16), green stars and blue triangles enclose another two trial regions. (b) Rectangular template region generation for improving V_T and three example trial regions for V_T improvement. (c),(d): Curve template generation for branch-wise initialisation improvement. Left (c): Basic line generation by rotation and point interpolation. Right (c): Generation of red basic template curves by fitting different number of points on the two basic lines with B-spline curves. Left (d): Generation of the curve templates by rotating the basic template curves into the second quadrant. Right (d): Production of multiple curve templates in the second quadrant by applying multiple angles θ_i uniformly distribute in the interval $[\alpha, \beta] = [-\pi/3, \pi/3]$ to the step (c)

$$\min_i \text{SL}_i = \sum_{j=1}^n l_{DP_{i,j}} \quad (16)$$

where $DP_{i,j}$ is the j th pixel of the dense pixels DP_i included in the i th template region. Each candidate set of pixels DP_i includes the same number of pixels n for fair searching. The procedures of the trial template generation and the principal direction improvement are illustrated in Figs. 4a and b.

With the improved principal directions V_T and V_N , the positions of the central five points on the boundaries of the heart region are obtained as illustrated in Fig. 3b, which are used to locate the coordinates of the other vessel branches with the Procrustes transformation. That is, finding the scaling coefficient b , rotation matrix T and translation matrix C such that

$$P = b \cdot RP \cdot T + C \quad (17)$$

where RP , P are the central five points of the pre-computed mean shape of the training shape database and the estimated shape, respectively. Parameters b , T , C are then applied to obtain the points on each vessel shape branch as follows:

$$Q_{i,j} = b \cdot RQ_{i,j} \cdot T + \frac{1}{n_i} \sum_{j=1}^{n_i} C_j \quad (18)$$

where RQ_i , Q_i record $n_i = 5$ points on the i th vessel branch of the mean and estimated shapes. Fig. 3c presents an estimated example shape.

For the last step, the vessel shape initialisation is further improved with branch-wise curve templates, i.e. deformed, rotated and translated parametric curves, to approximate vessel branches. For curve template generation, the vessel shape is divided into four parts with four quadrants using the optimised principal directions (V_T , V_N), and the central heart region is abandoned to reduce disturbance. Figs. 4c and d present the procedures of curve template generation and shape branch matching, then the best curve template achieved in (16) is chosen as the improved initialisation of the vessel branch in the corresponding quadrant, which is further employed for snake optimisation.

3.3 Abnormal shape elimination

After the shape initialisation or the snake optimisation, the obtained curve template may be abnormal if vessel branch texture does not exist in the considered quadrant. This abnormal vessel branch is replaced with the initialised average shape in (18). A vessel branch is determined to be abnormal if the average intersection angle $\text{AveAng} \geq (\pi/4)$ in (19) after shape initialisation or value $ov \geq (1/3) + (\pi/4)$ after snake optimisation

$$\begin{cases} \text{AveAng} = \frac{1}{n_i - 1} \sum_j \langle \text{Proc}V_{i,j}, \text{Opt}V_{i,j} \rangle, \\ ov = \frac{1}{n_i} \sum_j l_{\text{Opt}S_{i,j}} + \text{AveAng} \end{cases} \quad (19)$$

where $\langle \text{Proc}V_{i,j}, \text{Opt}V_{i,j} \rangle$ denotes the intersection angle between vectors of $\text{Proc}V_{i,j} = \text{Proc}S_{i,j+1} - \text{Proc}S_{i,j}$ and

Table 2 Module setting for different versions of algorithms

Algorithm	Input texture	Initialisation	Statement
AAM – G1I0 [13]	GGF (G_1) (17), (18) (I0)	Procrustes	for AAM, the preceding 40 images are chosen for training and the remaining are chosen for testing. To decrease the variation space of AAM, half the number of points on each vessel branch is employed for the training and testing
AAM – G0I1 [13]	smoothed image (G_0) templates (I1)	curve	
AAM – G1I1 [13]	GGF (G_1) templates (I1)	curve	
Snake – G1I0	GGF (G_1) (17), (18) (I0)	Procrustes	
Snake – G0I1	smoothed image (G_0) templates (I1)	curve	
Snake – G1I1	GGF (G_1) templates (I1)	curve	

$\text{Opt}V_{i,j} = \text{Opt}S_{i,j+1} - \text{Opt}S_{i,j}$, $\text{Proc}S$, $\text{Opt}S$ are the shapes obtained by Procrustes transformation (18) and curve templates (16) (or snake optimisation) and n_i is the number of points on the i th vessel branch. $l_{\text{Opt}S_{i,j}}$ is the lighting intensity on the pixel $\text{Opt}S_{i,j}$. Branch $\text{Opt}S_i$ has been scaled to have the same length as $\text{Proc}S_i$.

4 Experimental results

4.1 Database and experimental setting

We perform the experiments on a personal computer with a 3.2 GHZ core processor and 4 GB random access memory. A database of 72 embryo vessel images were used for the experiments, which were captured using 810 nm infrared lighting and a charge-coupled device camera by Co-Photoel Tech Co., Ltd. For each image, the ground truth heart region and each of the six main vessel branches in Fig. 1a are manually labelled with five uniformly distributed discrete points on interpolation curve. The manual marking up is done by a committee of three people including an initial marker, a checker from the university and a prover from the collaborating company. According to the image quality and shape complexity, the database is manually divided into three categories evenly: good, fair and poor.

To analyse the results quantitatively, a metric reflecting the bias between the located vessels and the ground truth is defined as follows:

$$\text{error} = \frac{(1/m \cdot n) \sum_{i,j} \| P_{i,j} - V_i \|_c}{\max_{i,j,k,l} \| V_{i,k} - V_{j,l} \|_2}, \quad (20)$$

where m, n are the numbers of vessels and the points on each branch, $P_{i,j}$ is the j th interpolated point on the i th located branch, $V_{i,k}$ is the k th point on the i th ground truth branch V_i , point and curve distance $\| p - \mathcal{L} \|_c$ is defined in (2). $\max_{i,j,k,l} \| V_{i,k} - V_{j,l} \|_2$ is the size of the vessel shape. The overall runtime metric RT of the considered algorithms is also considered for the comparison.

To analyse the effects of initialisation, GGF and the algorithm strategies, different versions of algorithms with each module considered are compared with the proposed model, which are presented in Table 2. The notation abbreviation $r1c2$ denotes the position of row one and column two.

4.2 Performance of GGF-based snake model

(i) *Comparison of initial shape prediction*: For the region extraction for the snake model, the popular level-set algorithm [6, 7] reported to be able to deal with the homogeneous effect in the segmentation problem, is also tested and compared with the self-adaptive thresholding method. Fig. 5 presents vessel regions extracted by the two algorithms on the smoothed images. It can be seen from the second row of Fig. 5 that though the level-set-based segmentation can find the vessel structure, it is sensitive to patch-like noise such as grey spot patches and introduces many

fragment patches that result in over-segmentation. The grey regions in the third row of Fig. 5 record the filtered regions by the self-adaptive thresholding method, which are more applicable for the skeletonisation method to filter out the long skeleton lines for snake optimisation initialisation.

(ii) *Comparison of snake model energies*: To evaluate the performance of the proposed snake model, three average energy terms in the objective function are compared including E_{line} in (5), E_{DirPre} in (7) and E_{LenPre} in (8). Three versions of snake algorithms are adopted for comparison including the original snake model (OriSnake), Snake – G0I1 and Snake – G1I1 in Table 2. The three energy values of these three snake models w.r.t. the number of iterations are presented in Fig. 6, in which OriSnake results in the largest and the most unstable direction and length energies, because it does not preserve the branch direction and length. Actually, lighting intensity term is negative correlation with the direction and length terms, though larger direction and length energies are obtained, Snake – G1I1 achieves smaller lighting intensity than Snake – G0I1 which illustrates that Snake – G1I1 is able to find a better curve branch by properly preserving the initial direction and length.

(iii) *Comparison of guidance fields*: To check the performance of the proposed GGF compared with other guidance fields, the gradient vector flow (GVF) [18] frequently used for closed boundary location [27] is employed for the comparison, which was proposed to deal with the cases of poor initialisation and boundary concavities. The average location errors of the snake model with GVF and GGF on the 24 good samples are 3.34 and 3.17%, respectively, which illustrate the effectiveness of the proposed GGF in overall. Fig. 7 shows an example that the evolution curve with GVF stagnates to a line which is far from the ground truth branch in the green rectangular region, whereas the curve converges to the ground truth branch successfully with the proposed GGF. As seen in right of Fig. 7a, the magnitude of the guidance force around the considered branch is much smaller than that around the heart region due to the misleading spot patches surrounding the considered branch, whereas GGF yields strong guidance information around the long ground truth line as shown in right Fig. 7b, since it integrates the distance apart from the longest skeleton line in a local region and the length of the skeleton line. This result indicates that the proposed GGF is more robust than GVF against small noisy spot patches, and it is more beneficial than GVF for facilitating the snake model to converge to true branch centrelines.

4.3 Comparison of algorithms for shape optimisation

Fig. 8 presents vessel shape branches detected by algorithms with different module settings in Table 2, where each three example images from each category are presented. Table 3 presents the quantitative results of the runtime, the location errors and the corresponding parameter settings of the algorithms.

Table 3 shows that the proposed snake model Snake – G1I1 provides the best performance among the algorithms with a reasonable runtime cost.

The effect of shape initialisation on the proposed models can be investigated by comparing the images in the third and fifth rows or the sixth and eighth rows in Fig. 8. As seen, a good shape initialisation is necessary for the open snake model; otherwise, the evolution curve may be trapped in the wrong local optimum [the sixth row and ninth column ($r6c9$) image], which is supported by the fact that the location errors of the algorithm Snake – G1I1 are smaller than those of Snake – G1I0 in Table 3.

The images in the fourth and fifth rows or the seventh and eighth rows of Fig. 8 are used to analyse the effect of the constructed GGF. Since the constructed GGF implies information regarding not only the distance apart from the target vessel branch but also the length of the skeleton line, it can push the evolution curve toward the optimal branch with long branch length. For example, the lower-right branch in $r7c7$ has been relocated to the optimum branch in $r8c7$. The effect of the GGF is further supported by the fact that an improvement of 0.12% is achieved by Snake – G1I1 compared with Snake – G0I1 on the fair images.

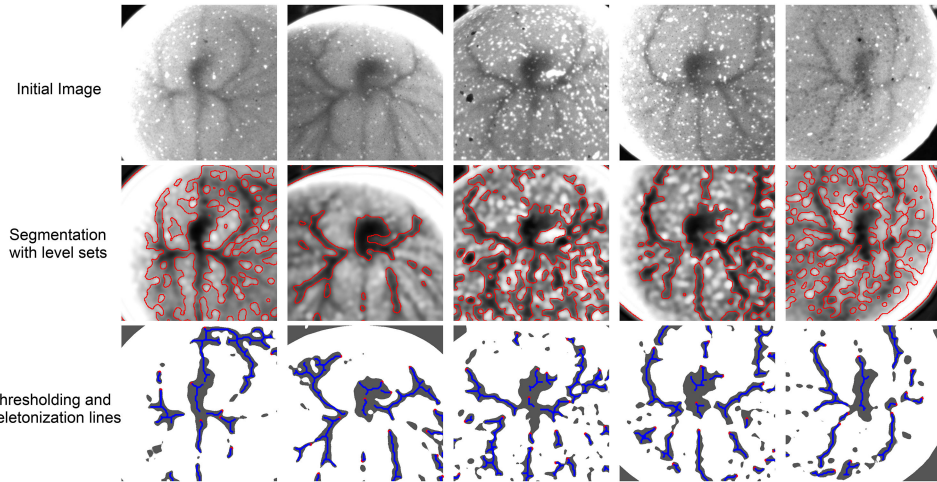


Fig. 5 Comparison of algorithms for initial shape prediction. From up to down, rows correspond to the initial images, the vessel shapes obtained by level-set segmentation and the self-adaptive thresholding method (blue lines denote the skeleton centre pixels)

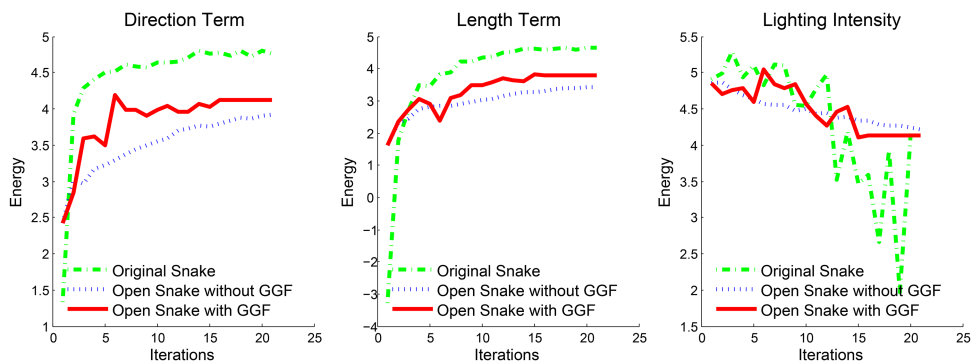


Fig. 6 Energies of direction, length and lighting intensity of three snake models w.r.t. the number of iterations

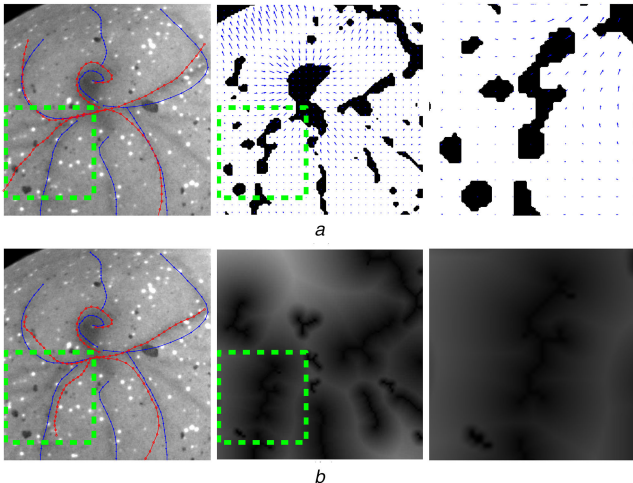


Fig. 7 Comparison of guidance fields GVF [18] and GGF for the open snake model **(a)**, **(b)**. Detection results and the used fields of GVF and GGF, respectively. The green rectangular region encloses the detected branch with large difference. The rectangular regions in central **(a)** and **(b)** are enlarged and presented in right of **(a)** and **(b)**, respectively

AAM [13] requires a shape and image database for model training. Even though shorter vessel branches are requested for the location than the snake optimisation, AAM rarely detects abnormally shaped vessel branches due to the restriction of the employed database such as the lower-left branch in *r5c6*. Concerning runtime costs, the snake model Snake – *G1I1* requires as much runtime as AAM – *G1I1* though the training runtime cost of AAM is not included, since the snake model uses only the derivatives of a set of discrete evolution points, rather than the derivatives w.r.t. texture pixels by AAM.

5 Discussion and conclusion

This paper proposes a new framework for locating embryo vessels which have three main novelties. First, an open snake preserving initial direction and length is proposed to locate open vessel branches. Second, a GGF incorporating not only the distance apart from the skeleton lines but also the length of the skeleton line is proposed, which can push the evolution curve toward the global optimum. Finally, shape initialisation based on deformation template matching is proposed for a specific application. Comparison to different algorithms demonstrates the competitiveness of the proposed GGF and model.

However, the proposed framework and models would benefit from further improvement. First, vessel shape initialisation should be made more general by considering the geometry features of the entire vessel shape. Our future work will apply the state-of-the-art deep learning method to improve the generalisation ability and efficiency of the shape initialisation. Additional applications of the proposed GGF and the open snake model such as the handwritten digit location shall be exploited as well.

6 Acknowledgments

The work was supported by the Natural Science Foundation of China under grant nos. 61272050, 61672357, 61602315 and 61402289, the China Postdoctoral Science Foundation under grant no. 2015M572363, the Science Foundation of Guangdong Province under grant nos. 2014A030313556 and 2014A030313558 and the open Foundation of Artificial Intelligence Key Laboratory of Sichuan Province under grant no. 2015RZY01.

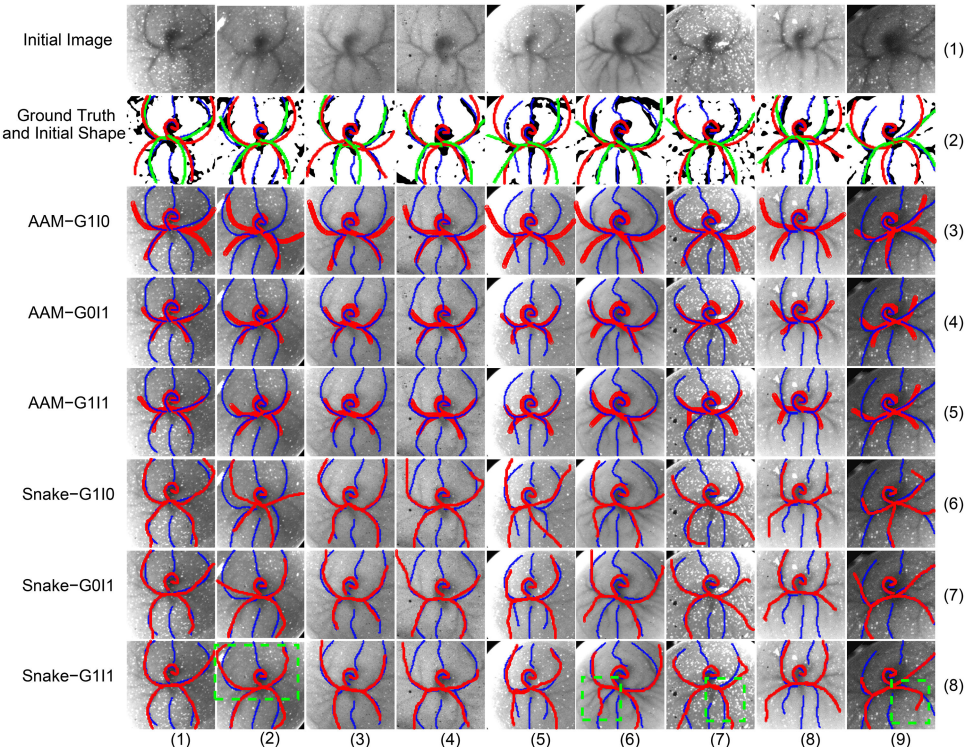


Fig. 8 Results of different algorithm versions. Red circles and blue stars denote the optimised and the ground truth shapes, respectively. For the images in the second row, the green and red lines denote the initialised shapes with Procrustes transformation and curve templates. The optimised branches with significant improvement are enclosed in green rectangular regions in the last row images

Table 3 Comparative results among different versions of AAM [13] and open snake models

Algorithm	RT, s	Location error			Parameter setting	
		Good	Fair	Poor		
Procrustes shape curve templates	≈ 0 1.4 ± 0.5	$12.16\% \pm 11.90\%$ $4.83\% \pm 3.93\%$	$13.02\% \pm 13.07\%$ $5.49\% \pm 3.65\%$	$14.06\% \pm 14.24\%$ $6.04\% \pm 3.63\%$	—	
AAM – G1I0	2.8 ± 0.4	$10.94\% \pm 10.48\%$	$9.98\% \pm 8.06\%$	$8.74\% \pm 9.54\%$	parameter setting in [13], $D = 120$	
AAM – G0I1	2.3 ± 0.4	$3.92\% \pm 2.57\%$	$4.18\% \pm 2.73\%$	$4.61\% \pm 3.05\%$	$\begin{cases} m = 3D, n = 10, \text{NumIter} = 20 \\ m = 3D, n = 3, \text{NumIter} = 20 \end{cases}$	
AAM – G1I1	2.7 ± 0.5	$3.74\% \pm 3.54\%$	$4.02\% \pm 3.22\%$	$4.48\% \pm 4.70\%$	the same as AAM – G1I0	
Snake – G1I0	3.3 ± 0.7	$8.42\% \pm 8.50\%$	$9.66\% \pm 12.24\%$	$10.48\% \pm 10.70\%$	$\alpha = 0.05, \beta = 0.05, \gamma = 0.5, \theta = 0.05, \eta = 0.1, \omega = 1000$	
Snake – G0I1	2.5 ± 0.8	$3.25\% \pm 2.05\%$	$3.41\% \pm 1.31\%$	$4.33\% \pm 1.73\%$	the same as Snake – G1I0	
Snake – G1I1	3.5 ± 0.6	$3.17\% \pm 1.38\%$	$3.32\% \pm 1.41\%$	$4.15\% \pm 1.58\%$	the same as Snake – G1I0	

The bold values indicate minimum location errors.

7 References

- [1] Kirbas, C., Quek, F.: ‘A review of vessel extraction techniques and algorithms’, *ACM Comput. Surv.*, 2004, **36**, (2), pp. 81–121
- [2] Bai, X., Latecki, L.J., Liu, W.: ‘Skeleton pruning by contour partitioning with discrete curve evolution’, *IEEE Trans. Pattern Anal. Mach. Intell.*, 2007, **29**, (3), pp. 449–462
- [3] Sezgin, M., Sankur, B.: ‘Survey over image thresholding techniques and quantitative performance evaluation’, *J. Electron. Imaging*, 2004, **13**, (1), pp. 146–168
- [4] Al-Rawi, M., Qutaishat, M., Arrar, M.: ‘An improved matched filter for blood vessel detection of digital retinal images’, *Comput. Biol. Med.*, 2007, **37**, (2), pp. 262–267
- [5] Zhao, Y.Q., Wang, X.H., Wang, X.F., et al.: ‘Retinal vessels segmentation based on level set and region growing’, *Pattern Recognit.*, 2014, **47**, (7), pp. 2437–2446
- [6] Li, C., Huang, R., Ding, Z., et al.: ‘A level set method for image segmentation in the presence of intensity inhomogeneities with application to MRI’, *IEEE Trans. Image Process.*, 2011, **20**, (7), pp. 2007–2016
- [7] Duan, J., Pan, Z., Yin, X., et al.: ‘Some fast projection methods based on chan-vese model for image segmentation’, *EURASIP J. Image Video Process.*, 2014, **2014**, (1), p. 7
- [8] Tan, L., Pan, Z., Liu, W., et al.: ‘Image segmentation with depth information via simplified variational level set formulation’, *J. Math. Imaging Vis.*, 2017, doi:10.1007/s10851-017-0735-3
- [9] Wang, Q., Boyer, K.L.: ‘The active geometric shape model: a new robust deformable shape model and its applications’, *Comput. Vis. Underst.*, 2012, **116**, (12), pp. 1178–1194
- [10] Geng, W., Cosman, P., Palm, M., et al.: ‘Caenorhabditis elegans egg-laying detection and behavior study using image analysis’, *EURASIP J. Appl. Signal Process.*, 2005, **14**, pp. 2229–2240
- [11] Geng, W., Cosman, P., Berry, C.C., et al.: ‘Automatic tracking, feature extraction and classification of *C. elegans* phenotypes’, *IEEE Trans. Biomed. Eng.*, 2004, **51**, (10), pp. 1811–1820
- [12] Lin, Z., Davis, L.S.: ‘Shape-based human detection and segmentation via hierarchical part-template matching’, *IEEE Trans. Pattern Anal. Mach. Intell.*, 2009, **32**, (4), pp. 604–618
- [13] Tzimiropoulos, G., Pantic, M.: ‘Optimization problems for fast AAM fitting in-the-wild’. Proc. IEEE Int. Conf. Computer Vision (ICCV), Sydney, Australia, 2013, pp. 593–600
- [14] Kass, M., Witkin, A., Terzopoulos, D.: ‘Snakes: active contour models’, *Int. J. Comput. Vis.*, 1988, **1**, (4), pp. 321–331
- [15] Li, H., Shen, T., Smith, M.B., et al.: ‘Automated actin filament segmentation, tracking and tip elongation measurements based on open active contour models’. Proc. IEEE Int. Symp. Biomedical Imaging: From Nano to Macro, Boston, MA, USA, 2009, pp. 1302–1305
- [16] Wang, Y., Narayanaswamy, A., Tsai, C., et al.: ‘A broadly applicable 3-D neuron tracing method based on open-curve snake’, *Neuroinformatics*, 2011, **9**, (2–3), pp. 193–217
- [17] Bresson, X., Esedoglu, S., Vandergheynst, P., et al.: ‘Fast global minimization of the active contour/snake model’, *J. Math. Imaging Vis.*, 2007, **28**, (2), pp. 151–167
- [18] Xu, C., Prince, J.L.: ‘Snakes, shapes, and gradient vector flow’, *IEEE Trans. Image Process.*, 1998, **7**, (3), pp. 359–369

- [19] Li, C., Liu, J., Fox, M.D.: ‘Segmentation of external force field for automatic initialization and splitting of snakes’, *Pattern Recognit.*, 2005, **38**, (11), pp. 1947–1960
- [20] Hou, Z., Han, C.: ‘Force field analysis snake: an improved parametric active contour model’, *Pattern Recognit. Lett.*, 2005, **26**, (5), pp. 513–526
- [21] Li, K., Lu, Z., Liu, W., *et al.*: ‘Cytoplasm and nucleus segmentation in cervical smear images using radiating GVF Snake’, *Pattern Recognit.*, 2012, **45**, (4), pp. 1255–1264
- [22] Meyer, F.G., Constable, R.T., Sinusas, A.J., *et al.*: ‘Tracking myocardial deformation using phase contrast MR velocity fields: a stochastic approach’, *IEEE Trans. Image Process.*, 1996, **15**, (4), pp. 453–465
- [23] Zhang, W., Pan, L., Tu, K., *et al.*: ‘Comparison of spectral and image morphological analysis for egg early hatching property detection based on hyperspectral imaging’, *PLoS One*, 2014, **9**, (2), p. e88659
- [24] Rez, P., Gangnet, M., Blake, A.: ‘Poisson image editing’, *ACM Trans. Graph.*, 2003, **22**, (3), pp. 313–318
- [25] Duan, J., Qiu, Z., Lu, W., *et al.*: ‘An edge-weighted second order variational model for image decomposition.’, *Digit. Signal Process.*, 2016, **49**, pp. 162–181
- [26] Weng, Y., Xu, W., Wu, Y., *et al.*: ‘2D shape deformation using nonlinear least squares optimization’, *Vis. Comput.*, 2006, **22**, (9–11), pp. 653–660
- [27] Zhou, H., Li, X., Schaefer, G., *et al.*: ‘Mean shift based gradient vector flow for image segmentation’, *Comput. Vis. Image Underst.*, 2013, **117**, (9), pp. 1004–1016